

Exchange interaction and demagnetization process of high-abundance rare-earth magnets sintered using dual alloy method

Dan Liu^{1,2*}, Tongyun Zhao^{2,3}, Jiaying Jin⁴, Tianyu Ma⁴, Jiefu Xiong³, Baogen Shen^{2,3*},
Fengxia Hu³, and Jirong Sun³

¹ Department of Physics, School of Artificial Intelligence, Beijing Technology and Business University, Beijing 100048, China;

² Ganjiang Innovation Academy, Chinese Academy of Sciences, Ganzhou 341000, China;

³ State Key Laboratory of Magnetism, Institute of Physics, Chinese Academy of Sciences, Beijing 100190, China;

⁴ School of Materials Science and Engineering, Zhejiang University, Hangzhou 310027, China

Received September 22, 2021; accepted November 30, 2021; published online February 17, 2022

The 2:14:1-type rare-earth (RE)-Fe-B permanent magnets prepared by the dual alloy method have been found to possess much superior magnetic properties to those prepared by the single alloy method, providing an appealing route to promote the utilization of high-abundance RE elements Ce and La and balance the use of the RE source. However, the relationship between magnetic interactions among different 2:14:1 main phases and superior magnetic properties is still unclear. In this study, we investigated the magnetic interactions and reversal field distribution in these magnets using first-order reversal curve (FORC) images. The FORC images showed that (Nd, Pr)_{27.8}(La, Ce)_{2.7}Fe_{bal}M_{1.4}B_{1.0} (S-9) and (Nd, Pr)_{19.5}(La, Ce)_{11.0}Fe_{bal}M_{1.4}B_{1.0} (S-36) have the characteristics of multiple main phases. The reverse magnetic fields corresponding to the soft and hard main phases, as well as the associated exchange coupling, were highly dependent on the LaCe content. The higher the LaCe content, the weaker the exchange coupling and the more asynchronous the demagnetization process. In addition, the FORC images indicated that the magnetization reversal process also varies with LaCe content, where the nucleation and propagation of reversed domains dominant in the S-9 magnet, while the domain propagation in the S-36 magnet is considerably suppressed. Additional micro-magnetic simulations also revealed that the coercivity and exchange coupling of multi-main-phase magnets decrease with increasing LaCe content, correlating well with the experimental results. These findings may not only contribute to a better understanding of the complex magnetic interactions between the soft and hard phases and how they affect macroscopic magnetic properties but also help in improving the magnetic performance of the RE-Fe-B magnets with high LaCe content.

permanent magnets, exchange interaction, first-order reversal curve, micromagnetism, high abundance rare-earth magnets

PACS number(s): 75.50.Ww, 71.70.Gm, 75.60.Jk, 91.25.Mf, 71.20.Eh

Citation: D. Liu, T. Zhao, J. Jin, T. Ma, J. Xiong, B. Shen, F. Hu, and J. Sun, Exchange interaction and demagnetization process of high-abundance rare-earth magnets sintered using dual alloy method, *Sci. China-Phys. Mech. Astron.* **65**, 247511 (2022), <https://doi.org/10.1007/s11433-021-1825-x>

1 Introduction

Permanent magnet materials are used in almost every in-

dustry because of their high coercivity and magnetic energy products [1-4]. As the most widely used permanent magnets, Nd-Fe-B-based magnets are essential in motors, generators, magnetic storage media, ore separators, and other electro-mechanical and electronic devices. However, the rapid consumption of the 2:14:1-type permanent magnets results in

*Corresponding authors (Dan Liu, email: liudan@btbu.edu.cn; Baogen Shen, email: shenbg@iphy.ac.cn)

the overuse and soaring prices of some rare-earth (RE) elements, such as Pr, Nd, Dy, and Tb. To make better use of resources and improve cost-effectiveness, La, Ce, Y, and other inexpensive and abundant RE elements are used to prepare $\text{RE}_2\text{Fe}_{14}\text{B}$ [5-8]. As the intrinsic magnetism of $\text{La}_2\text{Fe}_{14}\text{B}$ or $\text{Ce}_2\text{Fe}_{14}\text{B}$ is considerably less than that of $\text{Nd}_2\text{Fe}_{14}\text{B}$ or $\text{Pr}_2\text{Fe}_{14}\text{B}$, the substitution of Nd or Pr with La or Ce in the 2:14:1 phase lattice will seriously affect the performance of the magnet [9-11]. In general, the coercivity of permanent magnets depends on the intrinsic properties of the materials. However, when preparing high-abundance RE permanent magnets, the dual alloy method of mixing the soft and hard magnetic powders outperforms the traditional single alloy method. A multi-main-phase (MMP) magnet exhibits considerably better magnetic performance than a single-main-phase (SMP) magnet of the same composition [12,13]. This reveals that the deterioration in intrinsic magnetic properties of the $\text{RE}_2\text{Fe}_{14}\text{B}$ matrix phase is not the only reason for the degradation of high-abundance RE magnets.

An MMP magnet is a type of composite magnet that contains at least two main grains of different compositions. According to some studies, short-range exchange coupling between the hard and soft magnetic phases is detrimental to coercivity of sintered magnets [14,15]. In theory, however, the exchange coupling interaction between different grains can make the material possess the high coercivity of the hard phase and the high saturation magnetization of the soft phase [16]. The mixing of different powders results in a complex microstructure, such as a core-shell structure, for magnets sintered using the dual alloy method [17,18]. Exchange coupling exists not only between grains but also between cores and shells, influencing the magnetization reversal process. Therefore, the exchange coupling mechanisms of the MMP magnets and their influence on coercivity require further investigation.

The first-order reversal curve (FORC) is a magnetic measurement technique that aids the understanding of magnet exchange coupling and coercivity mechanisms. FORC can effectively reflect magnetization reversal process characteristics, such as qualitative and quantitative identification of magnetic phases, distribution of reversible and irreversible fields, and relative strength of interactions in magnets [19-21]. In this study, the sintered magnets of $(\text{Nd}, \text{Pr})_{27.8}(\text{La}, \text{Ce})_{2.7}\text{Fe}_{\text{bal}}\text{M}_{1.4}\text{B}_{1.0}$ and $(\text{Nd}, \text{Pr})_{19.5}(\text{La}, \text{Ce})_{11.0}\text{Fe}_{\text{bal}}\text{M}_{1.4}\text{B}_{1.0}$ ($\text{M} = \text{Al}, \text{Cu}, \text{Ga}, \text{Zr}$, wt.%) were prepared using the dual alloy method. The FORC technique was used to evaluate the magnetic properties and reversal field distribu-

tion between different main phases of the MMP magnets, which could provide a preliminary basis for understanding the magnetization reversal mechanism. In addition, the exchange energy and domain evolution during the demagnetization process were investigated in combination with the theory of micromagnetism. The micromagnetic method can directly observe the dynamic magnetization process of magnet materials as a bridge connecting the microstructure and macroscopic properties [22-24]. The exploration of the dynamic magnetization behavior of the MMP magnets has a substantial impact on improving magnetic performance and developing novel permanent magnets.

2 Experimental and simulation methods

As shown in Table 1, the alloys with the nominal compositions of $(\text{Nd}, \text{Pr})_{27.8}(\text{La}, \text{Ce})_{2.7}\text{Fe}_{\text{bal}}\text{M}_{1.4}\text{B}_{1.0}$ (S-9) and $(\text{Nd}, \text{Pr})_{19.5}(\text{La}, \text{Ce})_{11.0}\text{Fe}_{\text{bal}}\text{M}_{1.4}\text{B}_{1.0}$ (S-36) ($\text{M} = \text{Al}, \text{Cu}, \text{Ga}, \text{Zr}$, wt.%) were prepared using the dual alloy method. The S-9 and S-36 magnets were synthesized from $(\text{Nd}, \text{Pr})_{30.5}\text{Fe}_{\text{bal}}\text{M}_{1.4}\text{B}_{1.0}$ and $[(\text{Nd}, \text{Pr})_{0.5}(\text{La}, \text{Ce})_{0.5}]_{30.5}\text{Fe}_{\text{bal}}\text{M}_{1.4}\text{B}_{1.0}$ raw powders with the mass ratios of 82:18 and 28:72, respectively. Raw powders were prepared by induction melting, strip casting, hydrogen decrepitating, and jet milling. The powders were mixed and then pressed and aligned under 5.5 MPa pressure and 1.5 T magnetic field. Thereafter, the isostatic compacted compacts were sintered and annealed and a more detailed experimental procedures for the samples are described in ref. [17]. These two magnets were made into cuboids of 0.8 mm × 0.8 mm × 3 mm with a long geometric axis parallel to the z -axis. The samples were exposed to a magnetic field along its z -axis. The hysteresis loops and FORCs were measured using a superconducting quantum interference device vibrating sample magnetometer (SQUID-VSM, Quantum Design MPMS-3, China) at room temperature.

The theory of micromagnetism was used to investigate the exchange coupling mechanism and coercivity mechanism of permanent magnets. With the rapid development of numerical methods, comprehensive analysis of theoretical and experimental results can better reveal the relationship between the intrinsic properties and underlying mechanism of the magnets [25,26]. The total magnetic Gibbs free energy (E_{tot}) of the system can be expressed using eq. (1), where E_{ex} , E_{ani} , E_{d} , and E_{ext} are the exchange, anisotropy, demagnetization, and external field energies, respectively.

Table 1 Compositions of different samples

Multi-main-phase magnet	LaCe/RE content (wt.%)	Nominal composition
S-9	9	$(\text{Nd}, \text{Pr})_{27.8}(\text{La}, \text{Ce})_{2.7}\text{Fe}_{\text{bal}}\text{M}_{1.4}\text{B}_{1.0}$
S-36	36	$(\text{Nd}, \text{Pr})_{19.5}(\text{La}, \text{Ce})_{11.0}\text{Fe}_{\text{bal}}\text{M}_{1.4}\text{B}_{1.0}$

$$\begin{aligned}
E_{\text{tot}} &= E_{\text{ex}} + E_{\text{ani}} + E_{\text{d}} + E_{\text{ext}} \\
&= \int \left\{ A \left[(\nabla \mathbf{m}_x)^2 + (\nabla \mathbf{m}_y)^2 + (\nabla \mathbf{m}_z)^2 \right] \right. \\
&\quad \left. - K_1 \mathbf{m}_z^2 - \frac{1}{2} \mu_0 \mathbf{M} \cdot \mathbf{H}_{\text{d}} - \mu_0 \mathbf{M} \cdot \mathbf{H}_{\text{ext}} \right\} dV, \quad (1)
\end{aligned}$$

where A is the exchange integral constant, K_1 is the magnetocrystalline anisotropy constant, and V is the total volume of magnetic material. M denotes the magnetization state as a continuous function of position. $\mathbf{m}_x = \mathbf{M}_x/M_s$, $\mathbf{m}_y = \mathbf{M}_y/M_s$, and $\mathbf{m}_z = \mathbf{M}_z/M_s$ are the components of magnetization relative to the field direction. By solving the minimum energy of the three-dimensional finite element model, the demagnetization process and equilibrium magnetization configuration of the permanent magnet can be obtained.

3 Results and discussion

The intrinsic coercivity H_{cj} , remanence B_r , and maximum magnetic energy product $(BH)_m$ of the S-9 and S-36 magnets were shown in Table 2. Coercivity and magnetic energy product decreased from 13 kOe (1 Oe = 79.5775 A/m) and 47.9 MGOe to 9.6 kOe and 42.2 MGOe, respectively, as the LaCe content in the total RE content increased. To better analyze the demagnetization process and interaction mechanism of the MMP magnets, the FORC technique was employed [21]. Initially, the sample was magnetized to saturation in a specific direction. The external magnetic field was then decreased to a value less than the saturation field, denoted as a reverse magnetic field (H_R). A single FORC could be obtained by measuring the change curve of magnetization from H_R to the forward saturation field. By changing the H_R , a family of FORCs could be collected to cover the hysteresis loop. Figure 1 shows the FORCs of the S-9 and S-36 magnets. The curves presented in Figure 1(b) show a small step near zero field, suggesting that there is a

Table 2 Intrinsic coercivity H_{cj} , remanence B_r , and maximum magnetic energy product $(BH)_m$ of the S-9 and S-36 magnets

Multi-main-phase magnet	H_{cj} (kOe)	B_r (kGs)	$(BH)_m$ (MGOe)
S-9	13.0	14.0	47.9
S-36	9.6	13.4	42.2

small amount of soft phase (Ce-rich phase) uncoupled from the hard phase (Nd-rich phase) inside the magnet [21,27]. While the exchange coupling between the hard and soft phases improves as the LaCe content decreases (Figure 1(a)), it is generally believed that the coercivity mechanism of the RE-Fe-B magnets is mainly the nucleation and propagation of the reversed domain [28,29]. Moreover, because of the complex microstructure of the MMP magnet, the exchange coupling effect on magnetic domains during the demagnetization process cannot be overlooked. Reduced exchange coupling between different main phases is effective in slowing the expansion of reversed domains as the high-abundance RE content increases. Therefore, the combined effect of different mechanisms should be considered to understand the magnetization reversal process of the magnet more clearly.

Because the two-dimensional (2D) FORC distribution can record all irreversible magnetization processes, it is better adapted for understanding the demagnetization process and mechanism of the MMP magnets. The mixed second-order derivative of $M(H, H_R)$ concerning H and H_R is taken to obtain the normalized FORC distribution. Eq. (2) presents the distribution function of $M(H, H_R)$ on the (H, H_R) plane [30-32]:

$$\rho(H, H_R) = \frac{1}{2M_s} \frac{\partial^2 M(H, H_R)}{\partial H_R \partial H}. \quad (2)$$

The derivative ρ shown in Figure 2 is distributed on a 2D contour map with (H, H_R) as the coordinates. The external field is represented by the abscissa, while the reverse tran-

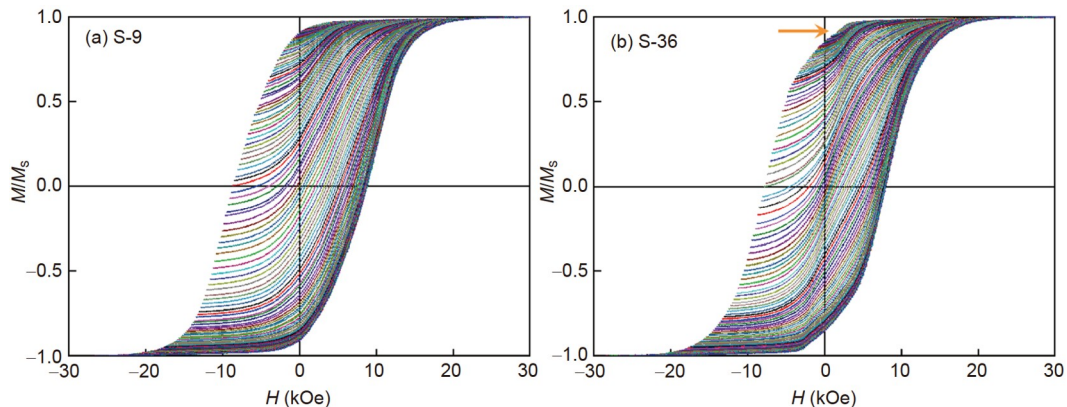


Figure 1 (Color online) First-order reversal curves (FORCs) of (a) S-9 and (b) S-36 at 300 K. A single FORC is obtained by measuring the change curve of magnetization from the reverse magnetic field to the forward saturation field. The orange arrow in (b) marks the location of the small step.

sition field is represented by the ordinate. When ρ is not zero, the mixed second-order derivative can remove all the completely reversible components of the magnetization reversal process, implying that the magnetization reversal is irreversible [33].

In contrast to the SMP magnet, where the RE elements are uniformly distributed in the 2:14:1 phase, the RE elements' concentration in the MMP magnet varies greatly even within the same main phase. Both S-9 and S-36 magnets exhibit the characteristics of multiple main phases, as shown in Figure 2, which are consistent with the electron probe microanalyzer (EPMA) results [17]. No obvious peak in the FORC distribution near the zero field shows that there is no completely decoupled soft magnetic phase in S-9. By contrast, there is a small amount of completely decoupled soft phase in S-36. This implies that the step shown in Figure 1(b) is primarily caused by decoupled grains with low anisotropy, which generally refers to surface grains, inhomogeneous grains, oxidized grains, and so on. Except for the zero field, there are two peaks in Figure 2(a) and (b) corresponding to different magnetization components. One peak located at the lower H corresponds to the irreversible magnetization of the soft phase, while the other peak corresponds to the irreversible magnetization of the hard phase. The reverse magnetic fields of these two peaks are 4.31 and 13.50 kOe for S-9 and 7.77

and 11.87 kOe for S-36, respectively.

The corresponding reverse transition field is close to coercivity when the contour line is parallel to the H -axis, as shown by the FORC distribution for S-9 (dashed blue line). When the contour line is perpendicular to the H -axis, the corresponding external field approaches coercivity (dashed red line). This characteristic of FORC suggests that the nucleation and expansion of reversed domains are the main mechanisms controlling the demagnetization process [20,34]. The exchange coupling inside the MMP magnet enhances the reverse transition fields of most Ce-rich grains, making the magnetization reversal process of the Ce- and Nd-rich grains more synchronous. With an increase in the LaCe content, the contour lines inside the red circle are inclined, indicating that the magnetization reversal of different grains becomes inconsistent. The completely uncoupled hard phase, depicted by the solid dotted circle on the lower right, is also increased, demonstrating that the exchange coupling between two phases is unsatisfactory. Furthermore, the distribution along the left diagonal direction in Figure 2(b) is more obvious than that in Figure 2(a), which shows the weakening of the exchange coupling effect within the S-36 magnet.

The 2D FORC contour map is a useful tool for recording the irreversible magnetization reversal in the (H , H_R) co-

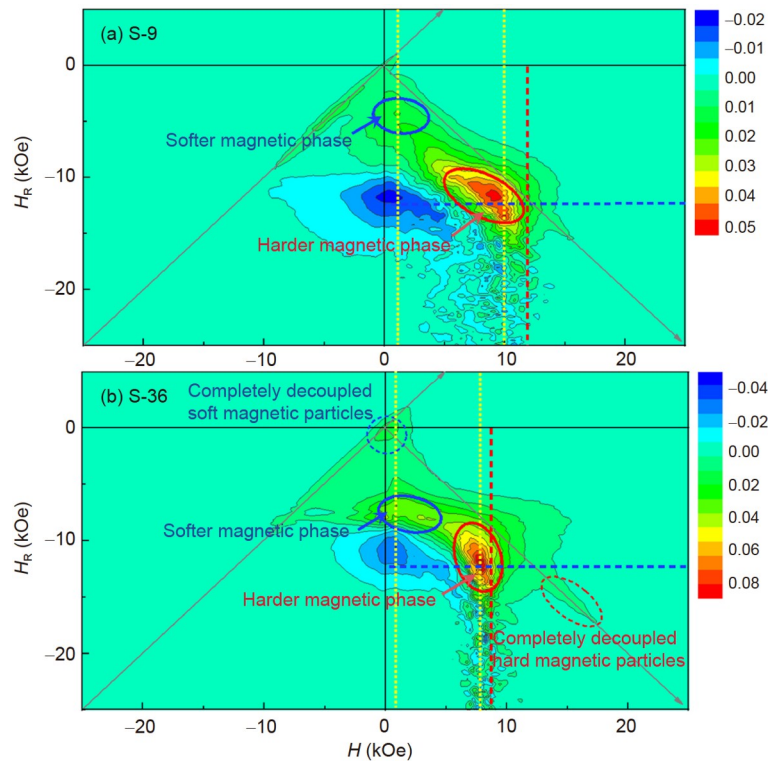


Figure 2 (Color online) Two-dimensional first-order reversal curve (FORC) distribution of (a) S-9 and (b) S-36. The corresponding FORC distributions are shown as contour plots after demagnetization correction, where the smoothing factor is 4. The arrows indicate the peaks corresponding to the magnetization reversals in the majority of Ce- and Nd-rich phases. The contour lines parallel and perpendicular to the H -axis are identified by the blue and red straight lines, respectively. The reverse field distribution of the soft and hard magnetic phases can be represented by the one-dimensional irreversibility distribution at the two dashed yellow lines (Figure 3).

ordinates. While the distribution of one-dimensional irreversibility aids in gaining a more intuitive understanding of the demagnetization inversion process, the integral of the derivative ρ concerning the external magnetic field H is also known as FORC-switching field distribution (SFD) [35]:

$$\int \frac{\partial^2 M(H, H_R)}{\partial H_R \partial H} dH = \frac{\partial M(H_R)}{\partial H_R}. \quad (3)$$

Figure 3 presents the effect of exchange coupling between the two main phases on magnetization reversal. The fluctuation of the curve near the high field indicates that the magnetization reversal of grains becomes inconsistent because of the change in internal interaction. The FORC-SFD is axisymmetric along the coercivity for a typical single-phase magnet [36]. However, the FORC-SFDs of S-9 and S-36 are not symmetrical and gradually deviate from the Gaussian symmetrical distribution along the direction of the small field. Magnetization reversal of the Ce-rich phase with low anisotropy occurs earlier in the demagnetization process, which is more visible in the S-36 magnet. The small protuberance near the zero field indicates that the S-36 magnet contains few uncoupled soft magnetic phases, corresponding to the small step on the demagnetization curve. While the peak at the zero magnetic field in the S-9 magnet is so weak that it is almost negligible, the two peaks near the coercivity shown in the inset of Figure 3(b) represent the inconsistency of the demagnetization process of different main phases.

Backscattered scanning electron microscopy (BSE-SEM) micrographs presented in Figure 3(c) and (d) show that the grain boundary (GB) phases in the magnet increase as the LaCe content increases, reducing the exchange coupling between the grains. Because of the weakening of the interaction within the magnet, the demagnetization of soft and hard magnetic phases is asynchronous, which supports the analysis of the FORC distribution.

The nucleation and propagation of reversed domains during demagnetization are further revealed via micromagnetic simulation. Centroidal Voronoi tessellation is used to model the multi-grain microstructure, which can well reflect the actual particle shape [37-39]. The model was meshed using the tetrahedral adaptive meshing method based on Delaunay algorithm. The model's macroscopic shape is a cube with a length of 3000 nm and 100 irregular grains, as shown in Figure 4(a). To simplify the model, $\text{Nd}_2\text{Fe}_{14}\text{B}$ and $(\text{Nd}_{0.5}\text{-Ce}_{0.5})_2\text{Fe}_{14}\text{B}$ were selected to represent the Nd- and Ce-rich grains, respectively. The ratios of these two grains in the S-9 and S-36 magnets are 82:18 and 28:72, respectively, which are consistent with the experiment. According to the BSE-SEM micrographs and corresponding elemental mappings of the MMP magnet sintered using the dual alloy method [17], the diffusion between grains cannot be ignored. Figure 4(b) presents a heterogeneous microstructure comprising the grains of varying compositions. There are two types of grains in the magnets: a soft $(\text{Nd}_{0.5}\text{Ce}_{0.5})_2\text{Fe}_{14}\text{B}$ core covered with a

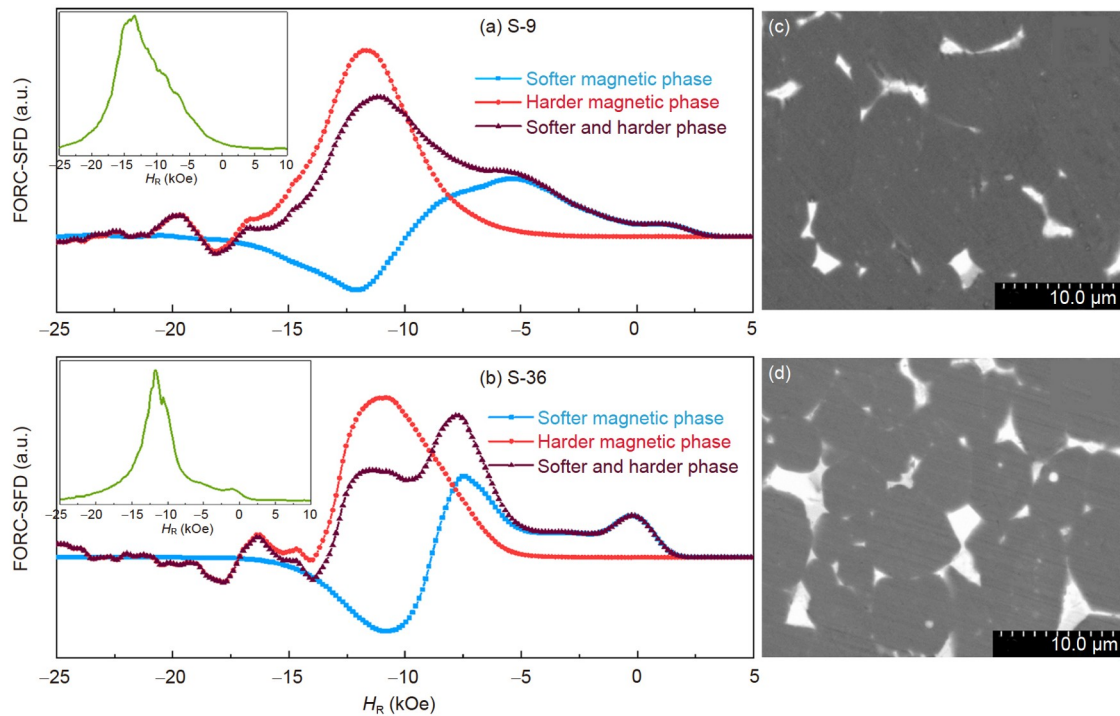


Figure 3 (Color online) First-order reversal curve-switching field distribution (FORC-SFD) of (a) S-9 and (b) S-36. The red- and blue-dotted plots are the reverse field distribution curves of the hard and soft magnetic phases at the dashed yellow lines shown in Figure 2. The total distribution curve is represented by the green line in the illustration. Backscattered scanning electron microscopy micrographs of the (c) S-9 and (d) S-36 magnets, with the bright and gray contrasts indicating the rare-earth-rich and matrix phases, respectively.

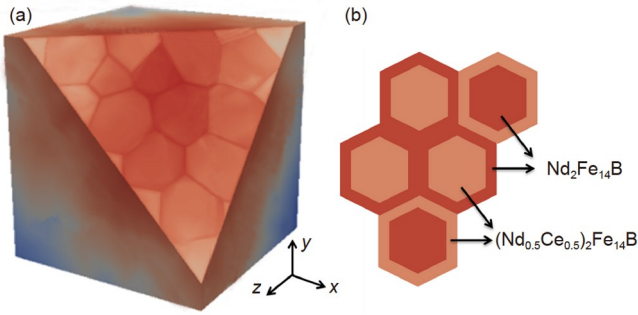


Figure 4 (Color online) (a) Polycrystalline model of multi-main-phase magnets created using the Voronoi tessellation method. (b) Schematic of the composition distribution of two types of grains with core-shell distributions. The overall size of the model is 3000 nm × 3000 nm × 3000 nm, and the model contains 100 irregularly shaped grains.

hard $\text{Nd}_2\text{Fe}_{14}\text{B}$ shell and a hard $\text{Nd}_2\text{Fe}_{14}\text{B}$ core covered with a soft $(\text{Nd}_{0.5}\text{Ce}_{0.5})_2\text{Fe}_{14}\text{B}$ shell. The thickness of an Nd- or a Ce-rich shell is defined as the shell width to grain-size ratio. For instance, a shell proportion of 0.03 indicates that the shell thickness is 3% that of the grain-size. The material parameters of $\text{Nd}_2\text{Fe}_{14}\text{B}$ and $(\text{Nd}_{0.5}\text{Ce}_{0.5})_2\text{Fe}_{14}\text{B}$ are presented in Table 3 [40,41].

Since it is difficult to observe the nucleation site experimentally, time-resolved simulations are used to resolve this issue. The simulated pattern sequence shown in Figure 5 presents the magnetization reversal process of S-9 and S-36 over time. The light colors (light red and light blue) represent the soft phase $(\text{Nd}_{0.5}\text{Ce}_{0.5})_2\text{Fe}_{14}\text{B}$ with different magnetization directions, while the dark colors (dark red and dark blue)

represent the hard phase $\text{Nd}_2\text{Fe}_{14}\text{B}$. On the right side of Figure 5, the corresponding demagnetization curves are presented. The calculated coercivity based on the two-phase model is usually greater than the experimental results because, from a micromagnetic standpoint, the artificially fabricated two-phase magnetic material comprises multiple phases. According to the comparison of Figure 5(a) and (b), the increase of Ce-rich grains in S-36 will affect its coercivity; however, S-36's coercivity is only 7% lower than that of S-9. This implies the decrease in coercivity can be prevented by optimizing grain microstructure. Magnetization reversal occurs preferably inside the $(\text{Nd}_{0.5}\text{Ce}_{0.5})_2\text{Fe}_{14}\text{B}$ grains rather than the $\text{Nd}_2\text{Fe}_{14}\text{B}$ grains. Then, the reversed domains propagate from one grain to another. As shown in Figure 5(a3) and (b2), some grains contain a portion of the reversed domain. Because of the differences in the chemical compositions between the core and shell regions, the magnetization reversal within a single grain is a gradual propagation process rather than a coherent rotation. Under a strong exchange coupling, the magnetic moments next to the soft phase in S-9 get reversed. In S-36, with weak exchange coupling, domain propagation between phases is inhibited, causing reversed domains to nucleate primarily at the soft magnetic phase and boundaries.

Moreover, it is discovered that the collective orientation of magnetic moments and the relative strength of energies are highly sensitive to magnet microstructure. Figure 6 presents the variation of coercivity and exchange coupling energy of S-9 and S-36 with a shell proportion and volume fraction of

Table 3 Magnetic properties of the Nd- and Ce-rich phases used in the simulation

Magnetic phase	Anisotropy constant K_1 (MJ/m ³)	Saturation magnetization $\mu_0 M_s$ (T)	Exchange stiffness A (pJ/m)
$\text{Nd}_2\text{Fe}_{14}\text{B}$	4.3	1.61	7.7
$(\text{Nd}_{0.5}\text{Ce}_{0.5})_2\text{Fe}_{14}\text{B}$	2.9	1.39	6.35

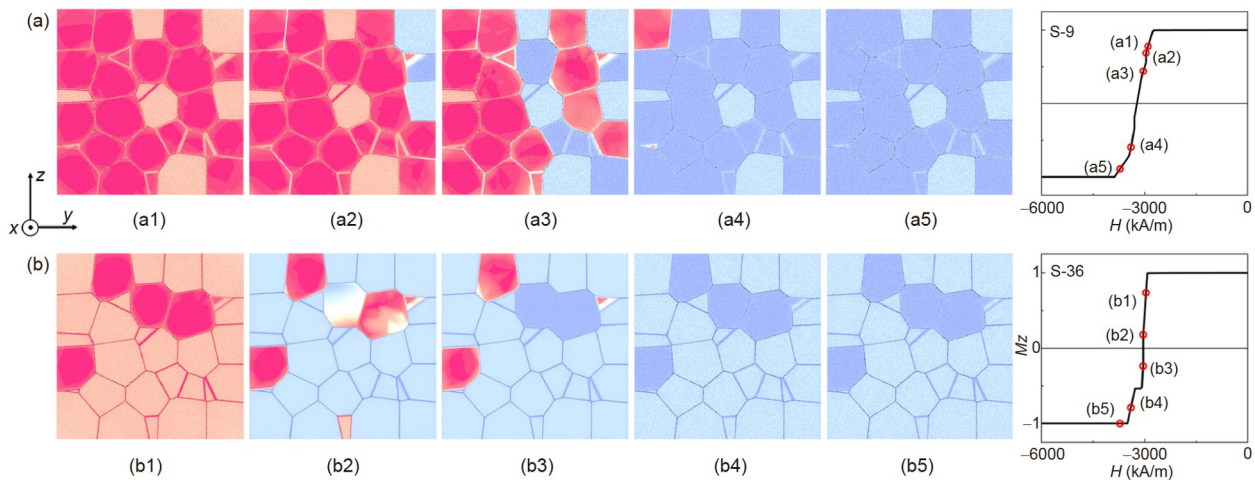


Figure 5 (Color online) Magnetization reversal patterns and corresponding demagnetization curves of the (a) S-9 and (b) S-36 magnets during the demagnetization process. The magnetization in the z -direction is represented by the regions in red (+ z) and blue (- z). The thickness of the Nd- or Ce-rich 2:14:1 shell is ~10 nm, which is 3% that of the average grain size.

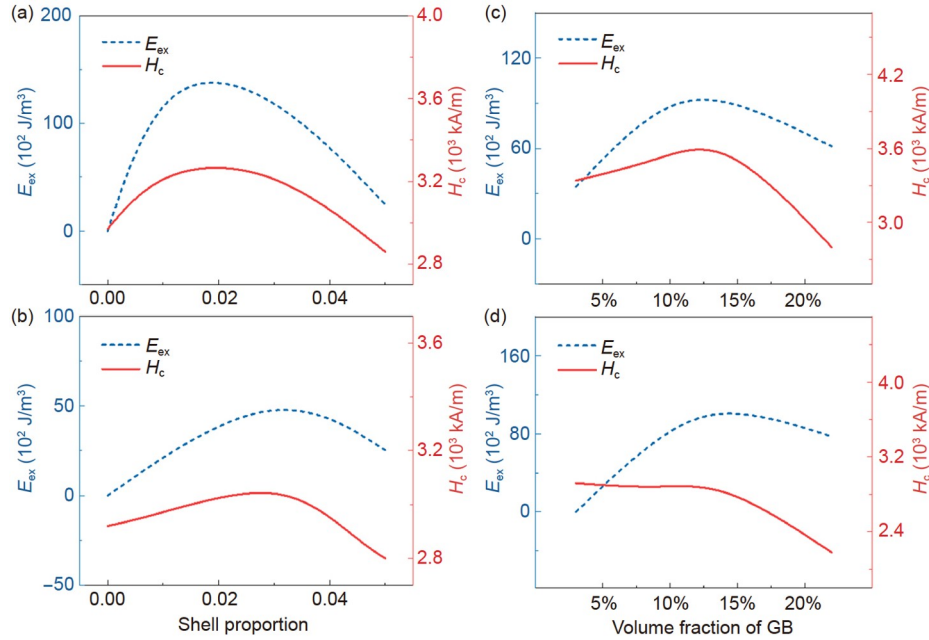


Figure 6 (Color online) Coercivity H_c and the corresponding exchange energy E_{ex} of (a) S-9 and (b) S-36 with different shell proportions. The shell proportion refers to the ratio of shell width to the average grain size. The effects of grain boundaries on the coercivity H_c and exchange energy E_{ex} of S-9 and S-36 are shown in (c) and (d), respectively.

the GB phase. E_{ex} is the exchange energy of the system near the coercive field. The GB phase was considered as an amorphous soft material characterized by $K_1 = 0 \text{ MJ/m}^3$, $\mu_0 M_s = 0.16 \text{ T}$ and $A = 6.0 \text{ pJ/m}$. As can be seen from Figure 6 that the variation trends of H_c and E_{ex} in different magnets are similar, which increase first and then decrease with increasing shell thickness or GB phase. This suggests that a moderate exchange coupling between grains is critical for improving magnetic performance.

The exchange coupling between the soft and hard phases is relatively weak in the absence of grain interdiffusion. At the beginning of the reversal processes, nucleation occurs in the soft magnetic phase and is then diffused to the hard magnetic phase. The exchange coupling and demagnetization of the magnets changed considerably when the grains transformed into a core-shell structure after diffusion. The core-shell structure plays three roles: (i) increasing the coercivity of the Ce-rich grains by improving the exchange interaction between different phases, (ii) using the structural advantage of a highly anisotropic shell surrounding a low anisotropic core to inhibit the reduction of coercivity, and (iii) weaken the effect of GB pinning, which poses a competitive relationship with (i). As reported, the high-performance high-abundance RE magnets can be obtained through structural optimization or ground boundary diffusion [42-44]. The grain microstructure changes to a core-shell structure when the boundaries between different main phases penetrate each other. However, deep diffusion may not be necessary for a core-shell structure owing to the gradual homogenization caused

by the overthick shell [18,45]. The diffusion processes of real magnets are considerably dependent on the surface quality and nature of the contact between the diffusion source and magnet and the core-shell structures should be formed while ensuring chemical heterogeneity.

4 Conclusions

The RE-Fe-B magnets with a high abundance of RE elements, such as Ce and La, have attracted attention owing to their role in promoting the balanced utilization of the RE resources. However, the exchange coupling mechanism and magnetization reversal process in magnets sintered using the dual alloy method need to be investigated further. FORC is used in this study to investigate the magnetic interactions and reversal field distribution in the MMP magnets. This shows that both S-9 and S-36 have the characteristics of multiple main phases, which is consistent with the EPMA results. The FORC image of S-9 shows that the nucleation and propagation of reversed domains are the primary mechanisms controlling the magnetization reversal process. Because of the weak exchange coupling, domain propagation is considerably suppressed in the S-36 magnet. In addition, the micromagnetic simulation results indicate that the coercivity and exchange coupling of the MMP magnets have a strong dependence on the LaCe content. Under strong exchange coupling, the magnetic moments next to the soft magnetic phase inside S-9 can be reversed, and the reversed domains

in S-36 are primarily nucleated at the soft magnetic phase and outer boundaries. Understanding the magnetic interaction between the soft and hard magnetic phases, as well as its impact on macroscopic magnetic properties, is crucial for improving the magnetic properties of the high-abundance RE magnets.

This work was supported by the Beijing Natural Science Foundation (Grant No. 2214070), Science Center of the National Science Foundation of China (Grant No. 52088101), National Natural Science Foundation of China (Grant Nos. 52001012, 51901057, U1832219, 51771223, and 51971240), Heye Chongming Project (Grant No. HYCMP-2021001), National Key Research and Development Program of China (Grant Nos. 2021YFB-3501202, 2021YFB35015043, 2020YFA0711502, 2019YFA0704900, 2018YFA0305704, and 2017YFA0303601), Key Projects of Capacity Construction of Science and Technology Innovation Service (Grant No. 19002020124), Beijing Talent Training Quality Construction Project (Grant No. 19008021064), Strategic Priority Research Program B (Grant No. XDB33030200), and Key Program of the Chinese Academy of Sciences (CAS). We thank Prof. Mi Yan from Zhejiang University for the kind help.

- 1 M. Sagawa, S. Fujimura, H. Yamamoto, Y. Matsuura, and K. Hiraga, *IEEE Trans. Magn.* **20**, 1584 (2003).
- 2 M. Liu, B. P. Han, G. B. Han, and R. W. Gao, *Sci. China-Phys. Mech. Astron.* **53**, 1590 (2010).
- 3 X. M. Song, Y. A. Zhang, Z. H. Dou, W. L. Pei, X. M. Ju, and L. Zhou, *Chin. J. Rare Metals* **45**, 163 (2021).
- 4 Y. Dong, H. Wang, B. J. Liu, X. Liu, J. X. Shang, Z. Q. Liu, T. L. Zhang, and C. B. Jiang, *Sci. China-Phys. Mech. Astron.* **64**, 247511 (2021).
- 5 T. Tomše, J. Jačimović, L. Herrmann, F. Greuter, R. Simon, S. Te-kavec, J. M. Dubois, and S. Kobe, *J. Alloys Compd.* **744**, 132 (2018).
- 6 E. B. Boltich, E. Oswald, M. Q. Huang, S. Hirose, W. E. Wallace, and E. Burzo, *J. Appl. Phys.* **57**, 4106 (1985).
- 7 X. Liao, J. Zhang, J. He, W. Fan, H. Yu, X. Zhong, and Z. Liu, *J. Mater. Sci. Tech.* **76**, 215 (2021).
- 8 Y. K. Zhang, S. H. Wang, K. Liu, D. G. Zhao, and C. Y. Song, *Chin. J. Rare Metals* **44**, 1215 (2020).
- 9 J. M. D. Coey, *Rare-Earth Iron Permanent Magnets* (Clarendon Press, Oxford, 1996).
- 10 M. Li, Y. Zhang, X. H. Wang, J. G. Yang, S. Qiao, S. L. Zheng, and Y. Zhang, *Rare Metals* **40**, 1 (2020).
- 11 D. Liu, T. Zhao, B. Shen, B. Li, M. Zhang, S. Zuo, J. Liu, S. Jiang, F. Hu, and J. Sun, *J. Alloys Compd.* **820**, 153098 (2020).
- 12 E. Niu, Z. A. Chen, G. A. Chen, Y. G. Zhao, J. Zhang, X. L. Rao, B. P. Hu, and Z. X. Wang, *J. Appl. Phys.* **115**, 113912 (2014).
- 13 Z. B. Li, B. G. Shen, M. Zhang, F. X. Hu, and J. R. Sun, *J. Alloys Compd.* **628**, 325 (2015).
- 14 T. Ma, B. Wu, Y. Zhang, J. Jin, K. Wu, S. Tao, W. Xia, and M. Yan, *J. Alloys Compd.* **721**, 1 (2017).
- 15 K. Hono, and H. Sepehri-Amin, *Scripta Mater.* **67**, 530 (2012).
- 16 E. F. Kneller, and R. Hawig, *IEEE Trans. Magn.* **27**, 3588 (1991).
- 17 J. Jin, T. Ma, Y. Zhang, G. Bai, and M. Yan, *Sci. Rep.* **6**, 32200 (2016).
- 18 T. Ma, M. Yan, K. Wu, B. Wu, X. Liu, X. Wang, Z. Qian, C. Wu, and W. Xia, *Acta Mater.* **142**, 18 (2018).
- 19 L. C. C. Arzuza, F. Béron, and K. R. Pirota, *J. Magn. Magn. Mater.* **534**, 168008 (2021).
- 20 R. K. Dumas, C. P. Li, I. V. Roshchin, I. K. Schuller, and K. Liu, *Phys. Rev. B* **75**, 134405 (2007).
- 21 I. D. Mayergoyz, and G. Friedman, *IEEE Trans. Magn.* **24**, 212 (1988).
- 22 W. F. Brown, *Micromagnetics* (Wiley Interscience, New York, 1963).
- 23 D. Liu, T. Zhao, M. Zhang, L. Wang, J. Xi, B. Shen, B. Li, F. Hu, and J. Sun, *J. Mater. Sci.* **56**, 4677 (2021).
- 24 T. Schrefl, G. Hrkac, S. Bance, D. Suess, O. Ertl, and J. Fidler, *Numerical Methods in Micromagnetics (Finite Element Method)* (Wiley, New York, 2007).
- 25 G. P. Zhao, H. W. Zhang, Z. Y. Zhong, and L. Chen, *Sci. China-Phys. Mech. Astron.* **54**, 1249 (2011).
- 26 Y. W. Liu, and Z. Z. Zhang, *Sci. China-Phys. Mech. Astron.* **56**, 184 (2013).
- 27 J. E. Davies, O. Hellwig, E. E. Fullerton, J. S. Jiang, S. D. Bader, G. T. Zimányi, and K. Liu, *Appl. Phys. Lett.* **86**, 262503 (2005).
- 28 L. I. Bo, J. F. Hu, D. Wang, B. Guo, and X. Wang, *Rare Metals* **23**, 152 (2004).
- 29 S. L. Chen, W. Liu, and Z. D. Zhang, *Phys. Rev. B* **72**, 224419 (2005).
- 30 C. R. Pike, A. P. Roberts, and K. L. Verosub, *J. Appl. Phys.* **85**, 6660 (1999).
- 31 H. G. Katzgraber, F. Pazmandi, C. R. Pike, K. Liu, R. T. Scalettar, K. L. Verosub, and G. T. Zimanyi, *Phys. Rev. Lett.* **89**, 257202 (2002).
- 32 W. Liu, and Z. Zhang, *Chin. Phys. B* **26**, 117502 (2017).
- 33 J. Olamit, K. Liu, Z. P. Li, and I. K. Schuller, *Appl. Phys. Lett.* **90**, 032510 (2007).
- 34 J. E. Davies, O. Hellwig, E. E. Fullerton, M. Winklhofer, R. D. Shull, and K. Liu, *Appl. Phys. Lett.* **95**, 022505 (2009).
- 35 R. K. Dumas, Y. Fang, B. J. Kirby, C. Zha, V. Bonanni, J. Nogués, and J. Åkerman, *Phys. Rev. B* **84**, 054434 (2011).
- 36 J. F. Xiong, R. X. Shang, Y. L. Liu, X. Zhao, W. L. Zuo, F. X. Hu, J. R. Sun, T. Y. Zhao, R. J. Chen, and B. G. Shen, *Chin. Phys. B* **27**, 077504 (2018).
- 37 Q. Du, V. Faber, and M. Gunzburger, *SIAM Rev.* **41**, 637 (1999).
- 38 R. Quey, P. R. Dawson, and F. Barbe, *Comput. Methods Appl. Mech. Eng.* **200**, 1729 (2011).
- 39 W. Scholz, J. Fidler, T. Schrefl, D. Suess, R. Dittrich, H. Forster, and V. Tsiantos, *Comput. Mater. Sci.* **28**, 366 (2003).
- 40 T. Schrefl, R. Fischer, R. Fidler, and H. Kronmüller, *J. Appl. Phys.* **76**, 7053 (1994).
- 41 J. F. Herbst, *Rev. Mod. Phys.* **63**, 819 (1991).
- 42 J. Jin, Z. Wang, G. Bai, B. Peng, Y. Liu, and M. Yan, *J. Alloys Compd.* **749**, 580 (2018).
- 43 H. X. Zeng, Z. W. Liu, J. S. Zhang, X. F. Liao, and H. Y. Yu, *J. Mater. Sci. Tech.* **36**, 50 (2020).
- 44 J. Jin, M. Yan, W. Chen, W. Zhang, Z. Zhang, L. Zhao, G. Bai, and J. M. Greneche, *Acta Mater.* **204**, 116529 (2021).
- 45 T. Ma, W. Zhang, B. Peng, Y. Liu, Y. Chen, X. Wang, and M. Yan, *J. Phys. D-Appl. Phys.* **51**, 055003 (2018).